# Template-Free Synthesis of Hollow-Structured Co₃O₄ Nanoparticles as High-Performance Anodes for Lithium-Ion Batteries

Deli Wang,*,† Yingchao Yu,‡ Huan He,† Jie Wang,† Weidong Zhou,‡ and Hector D. Abruña*,‡

†School of Chemistry and Chemical Engineering, Key Laboratory for Large-Format Battery Materials and System, Ministry of Education, Huazhong University of Science & Technology, Wuhan, 430074, People's Republic of China and ‡Department of Chemistry and Chemical Biology, Cornell University, Ithaca, New York 14853, United States

**ABSTRACT** We have developed a template-free procedure to synthesize $Co_3O_4$ hollow-structured nanoparticles on a Vulcan XC-72 carbon support. The material was synthesized *via* an impregnation—reduction method followed by air oxidation. In contrast to spherical particles, the hollow-structured $Co_3O_4$ nanoparticles exhibited excellent lithium storage capacity, rate capability, and cycling stability when used as the anode material in lithium-ion batteries. Electrochemical testing showed that the hollow-structured $Co_3O_4$



particles delivered a stable reversible capacity of about 880 mAh/g (near the theoretical capacity of 890 mAh/g) at a current density of 50 mA/g after 50 cycles. The superior electrochemical performance is attributed to its unique hollow structure, which combines nano- and microscale properties that facilitate electron transfer and enhance structural robustness.
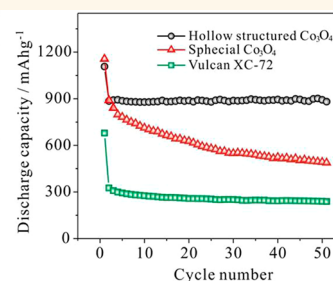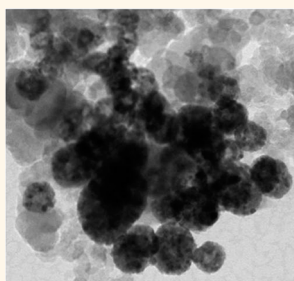
**KEYWORDS:** cobalt oxides · hollowed structure · anode materials · lithium battery · electrochemistry

Transition metal oxides (TMOs) have attracted great attention as anode materials to replace the currently used graphite, in order for lithium-ion batteries (LIBs) to achieve higher energy and power densities.[1−3] The attractive electrochemical performance of TMOs in LIBs is based on a conversion reaction mechanism, which is different from the conventional Li⁺ intercalation/deintercalation processes.[3,4] Among these, cobalt oxide ($Co_3O_4$) is one of the most widely studied materials due to its high theoretical capacity (890 mAh/g) and stable electrochemical performance during LIB operation. More interestingly, depending on the growth conditions, the shape and size of $Co_3O_4$ can be tuned. Numerous examples can be found in the literature on the synthesis of $CoO_x$ materials with novel structures, including nanotubes,[5] nanorods,[6] nanocubes,[7] nanowires,[8] nanosheets,[2] hollow-structured nanoparticles,[9−14] and hierarchically nanostructured nanoparticles.[15−19]

To date, the search for suitable candidates as anode materials in LIBs to replace graphite requires a strategic material structure design, which still relies on finding an appropriate morphology that can fulfill the following criteria: (a) fast Li⁺ transport; (b) sufficient space for potential volume expansion; (c) mechanical robustness; and (d) high surface-to-volume ratio. Hollow-structured nanomaterials have gained much attention in many aspects of electrochemistry such as fuel cells,[20−24] supercapacitors,[25,26] and LIBs.[11,12,16,27,28] The enhanced electrochemical performance of hollow-structured nanomaterials is attributed at least in part to their high surface area and surface to volume ratio. It has been reported that the voids inside hollow nanoparticles can not only provide more space to accommodate volume changes during charge/discharge but also shorten the Li⁺ diffusion distance, which leads to smaller overpotentials and faster reaction kinetics at the electrode surface.[27,29] The most commonly used method

for synthesizing hollow nanoparticles is the template-assisted method. This involves the coating of the desired materials onto sacrificial templates, followed by selective removal of the templates.[30−35] Another method is to use electrophoretic deposition to directly create hollow $Co_3O_4$ particles on a current collector.[16] However, most of these approaches involve complex synthetic strategies, which are costly and time-consuming. Moreover, the yield is often on the scale of milligrams to grams, limiting their application for large-scale production for LIBs.

Here, we describe a one-pot, two-step method to synthesize hollow $Co_3O_4$ nanoparticles dispersed on a Vulcan XC-72 carbon support. The hollowed structure was verified by high-angle annular dark field and bright field scanning transmission electron microscopy (HAADF- and BF-STEM) imaging. Electrochemical testing indicates the hollow-structured $Co_3O_4$ nanoparticles exhibited excellent lithium storage capacity, rate capability, and cycling stability compared with special $Co_3O_4$ nanoparticles when used as the anode material in lithium-ion batteries. The synthesis was accomplished *via* an all-solid-state method, producing the active materials on a carbon support in one pot on a lab bench and can potentially be scalable to large quantities for industrial production.

## RESULTS AND DISCUSSION

An impregnation−reduction method[36−38] ($CoCl_2 \rightarrow$ Co) was employed followed by an air-oxidation procedure (Co $\rightarrow Co_3O_4$). As illustrated in Figure 1, the $CoCl_2$ precursor was first dispersed on the Vulcan XC-72 carbon support and then reduced under flowing $H_2$ in a tube furnace at 300 °C. After cooling to room temperature under a $N_2$ atmosphere, the metallic cobalt nanoparticles supported on carbon (Co/C) were collected. The as-prepared Co/C nanoparticles were then heat-treated in a tube furnace under open air at a ramp rate of 1 °C/min up to 400 °C for 10 h to form hollow-structured $Co_3O_4$ nanoparticles (see more details in the experimental section of the Supporting Information). The voids were created during air heating, as a result of the Kirkendall effect:[39] the diffusion rates of cations and anions are not the same in the nanoparticle. A recent work has investigated, in detail, the hollowing mechanism of a similar system,[40] attributing it to the different diffusion rates of Co and O *via* a two-step mechanism. A similar hollowing phenomenon can also be observed in the Fe system.[41] An optimal heat-treatment temperature was chosen based on thermogravimetric analysis (TGA) of the Co/C in air (Figure S1, Supporting Information). X-ray diffraction (XRD) shows (Figure 1) a phase transformation from pure metallic Co to the spinel cobalt oxide phase ($Co_3O_4$). The diffraction peaks at $2\theta = 41.7°$, 44.5°, and 47.5° can be indexed to the (100), (002), and (101) planes, respectively, corresponding to the hexagonal phase of Co
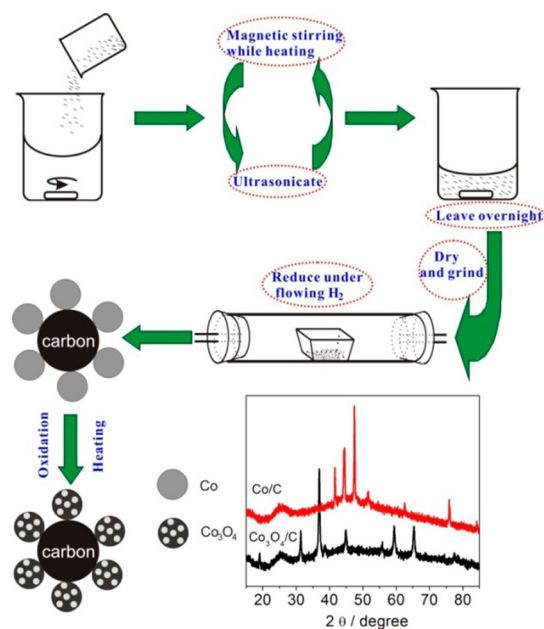


**Figure 1.** Schematic illustration of the synthesis procedure of Co/C and hollow structured $Co_3O_4$/C nanoparticles and the XRD patterns of Co/C and $Co_3O_4$/C.

(JCPDS: 05-0727).[42,43] The XRD patterns of metallic Co show a dramatic transition after heat treatment under open air. The diffraction peaks at $2\theta = 31.3°$, 36.9°, 44.9°, 59.4°, and 65.4° are indexed to (220), (311), (400), (511), and (440) planes, respectively, matching with that of the cubic spinel $Co_3O_4$ (JCPDS: 42-1467).[44,45] These results demonstrate the complete conversion of $CoCl_2$ to metallic Co and then to $Co_3O_4$.

To understand the microstructure of the as-synthesized hollow $Co_3O_4$/C material, we performed high-angle annular dark field and bright field scanning transmission electron microscopy (HAADF- and BF-STEM) imaging, shown in Figures 2a,b. Typical nanoparticles had diameters ranging from 50 to 100 nm, with nanoparticle pore sizes ranging from 10 to 50 nm. All of the $Co_3O_4$ nanoparticles exhibited a hollow structure with a rough surface, in contrast to the metallic cobalt nanoparticles, which all showed a nonhollow structure (Figure S2, Supporting Information). A detailed view of one hollow nanoparticle is presented in Figure 2c,d, with an oval-shaped pore shown clearly at the center, surrounded by multiple small vacancies. We suspect that this 50 nm nanoparticle was formed by the coarsening of several smaller nanoparticles, each less than 10 nm in size (Figures 2c). On one hand, this large pore fraction greatly increases the surface-to-volume ratio, enabling more active material to participate in the electrochemical reaction. On the other hand, the interconnected structure should provide pathways for the diffusion of $Li^+$, facilitating charge transfer. The energy-dispersive X-ray (EDX) line profile (Figure 2e) shows that both the Co and O signals decrease in the middle in the void as expected. The EDX map in Figure 2f−h show

that the Co to O ratios are uniform across the particles, as expected for a single phase. Such a combination of pores and vacancies is desirable for superior electrochemical performance, since it not only shortens the diffusion distance for $Li^+$ and electrons but also
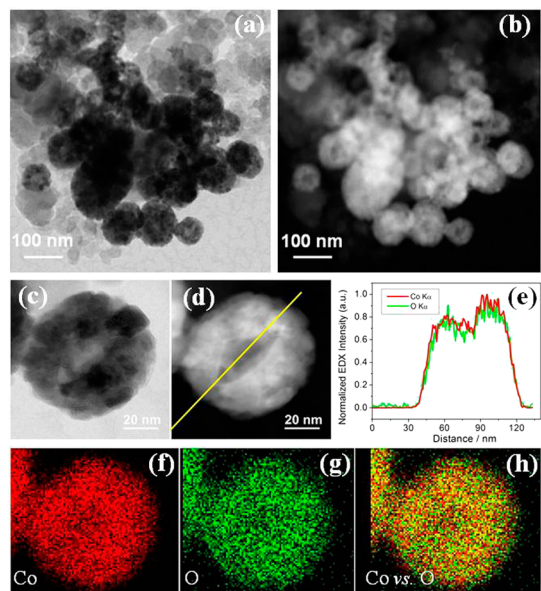


**Figure 2. Microstructure analysis of the as-prepared hollow Co₃O₄/C. (a, b) HAADF and BF STEM of the overview images. (c, d) HAADF and BF STEM of a detailed nanoparticle, along with (e) EDX line profile of Co (red) and O (green), showing the decrease of intensity of concentration in the middle. (f, g) EDX mapping of Co and O, respectively, and (h) overlay showing the homogeneous distribution of Co and O.**

mitigates the volume expansion and the stresses during charge/discharge.

The electrochemical performance of the hollow Co₃O₄/C was performed in 2032 coin cells with Li foil as the counter electrode. Figure 3a shows a typical discharge−charge profile of the hollow-structured Co₃O₄ nanoparticles with a cutoff voltage of +0.05 V *vs* Li at a current density of 50 mA/g. To accurately establish the capacity from only the active material Co₃O₄ and exclude the contribution from the carbon support material Vulcan XC-72, we measured the loading of Co₃O₄ on a carbon support *via* TGA (Figure S3, Supporting Information), and from the weight loss of the carbon support, we determined 55% Co₃O₄ loading by weight. In addition, we calculated the capacity as a result of the addition of Vulcan XC-72, shown as the green plot in Figure 3c. Using the following equation, we can determine the capacity derived only from Co₃O₄.

$$C_{Co_3O_4} = \frac{Q_{total} - C_C \times m_C}{m_{Co_3O_4}} \qquad (1)$$

where $C_{Co_3O_4}$ is the mass specific capacity of Co₃O₄ (the unknown), $Q_{total}$ is the measured coulomb charge, $m_{Co_3O_4}$ is the mass of Co₃O₄ (obtained from TGA, Supporting Information Figure S3), $C_C$ is the mass specific capacity of the carbon support (obtained *via* a control experiment, Figure 3c, the capacity of pure Vulcan XC-72), and $m_c$ is the mass of Vulcan XC72 (total material mass minus the mass of Co₃O₄). Equation 1 is robust when there is a carbon additive involved
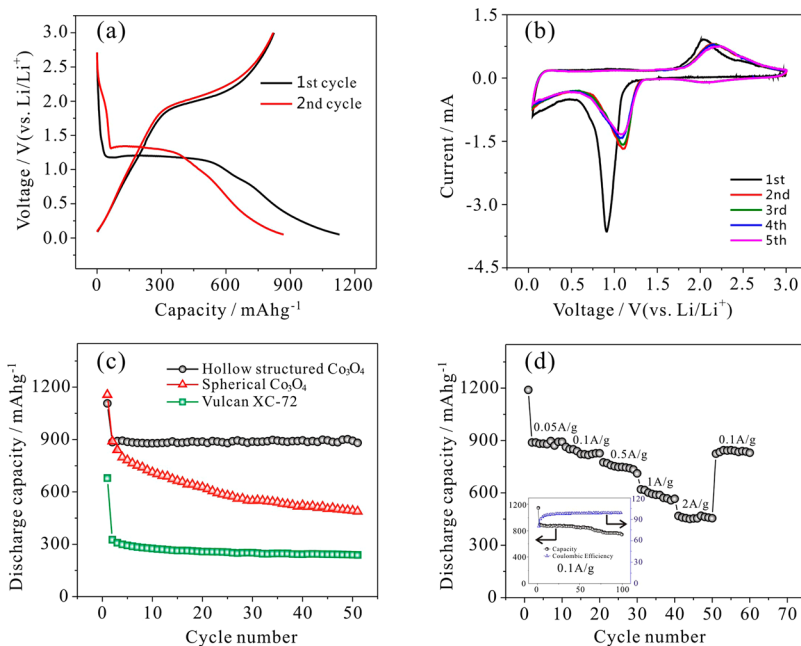


**Figure 3. Electrochemical performance of hollow Co₃O₄/C. (a) Charge and discharge profiles of the first and second cycles. (b) Cyclic voltammetry of the first five cycles. (c) Comparison of discharge capacity of hollow-structured Co₃O₄/C, special Co₃O₄/C, and Vulcan XC-72. (d) Discharge capacity at various current densities. Note 50 mA/g is about 0.05C (1C is about 890 mA/g). The inset in (d) shows the cyclability and corresponding Coulombic efficiency of hollow-structured Co₃O₄/C at a current of 100 mA/g.**

(for example, carbon black). As a comparison, without the correction of carbon support, we would report a stabilized capacity of 1140 mAh/g, which is about 250 mAh/g higher than its theoretical capacity. We thus believe that the capacity correction is necessary for anode material mixed with carbon upon being discharged to lower voltage.

The voltage capacity profile in Figure 3a shows a discharge plateau at about +1.1 V (*vs* Li) for the first cycle and about +1.2 V for the second cycle, with a high initial capacity of 1107 mAh/g, which dropped to 880 mAh/g after the second cycle. The irreversible capacity loss is frequently attributed to the decomposition of electrolytes and the formation of a solid−electrolyte interface (SEI) on the surface of the electrode materials[46,47] or an irreversible conversion process. Figure 3b shows cyclic voltammograms (CVs) of electrodes made from the hollow $Co_3O_4$ nanoparticles in a coin cell at a scan rate of 0.05 mV/s. The first cathodic scan exhibits an irreversible reduction peak at around +0.88 V, in good agreement with the irreversible capacity loss in Figure 3a. After the first scan, the cathodic peak shifts to about +1.2 V and a corresponding anodic peak to about +2.1 V. Few changes were observed from the second cycle to the fifth cycle, indicating good cycling stability. At a relatively low current density of 50 mA/g (1C is about 890 mA/g), the reversible capacity of the hollow-structured $Co_3O_4$ nanoparticles was around 880 mAh/g (Figure 3c), which is very close to the theoretical capacity of 890 mAh/g. Such capacity is much higher than that of spherical $Co_3O_4$ nanoparticles

(about 450 mAh/g after 50 cycles, Figure 3c). Compared to a Li-intercalated Vulcan XC72 carbon support (Figure 3c), the hollow $Co_3O_4$ exhibited about 3 times higher capacity. Reversible capacities of 850, 750, 600, and 450 mAh/g are observed after increasing the discharge/charge current density to 100, 500, 1000, and 2000 mA/g, respectively (Figure 3d). Notably, after 50 cycles at varied current densities, the capacity could be restored to 880 mAh/g when the current density was reset to 50 mA/g. Furthermore, when the current density was increased to 100 mA/g, the discharge capacity can still be stabilized at about 770 mAh/g after 100 cycles, as shown in the inset of Figure 3d. The first cycle Coulombic efficiency of hollow $Co_3O_4$/C is about 80%, then quickly increased to around 90% for the second cycle and stabilized at a value of 98.5% after several cycles as shown in the inset of Figure 3d. These data demonstrate that the hollow $Co_3O_4$ could be a promising candidate for anode material for LIBs.

Electrochemical impedance spectroscopy (EIS) was used to further explore the reason for the observed good cycling stability of hollow $Co_3O_4$/C materials and to analyze electrode kinetics of the different cells. Figure 4 compares the Nyquist plots and corresponding Bode plots of three fresh coin cells using Vulcan XC-72 carbon (C), spherical $Co_3O_4$/C, and hollow-structured $Co_3O_4$/C as electrode materials, respectively. The measurements were carried out over the frequency range from 100 kHz to 0.01 Hz at the open-circuit potential. For the fresh cells (Figure 4a), all three EIS curves for the fresh cells consist of a depressed semicircle
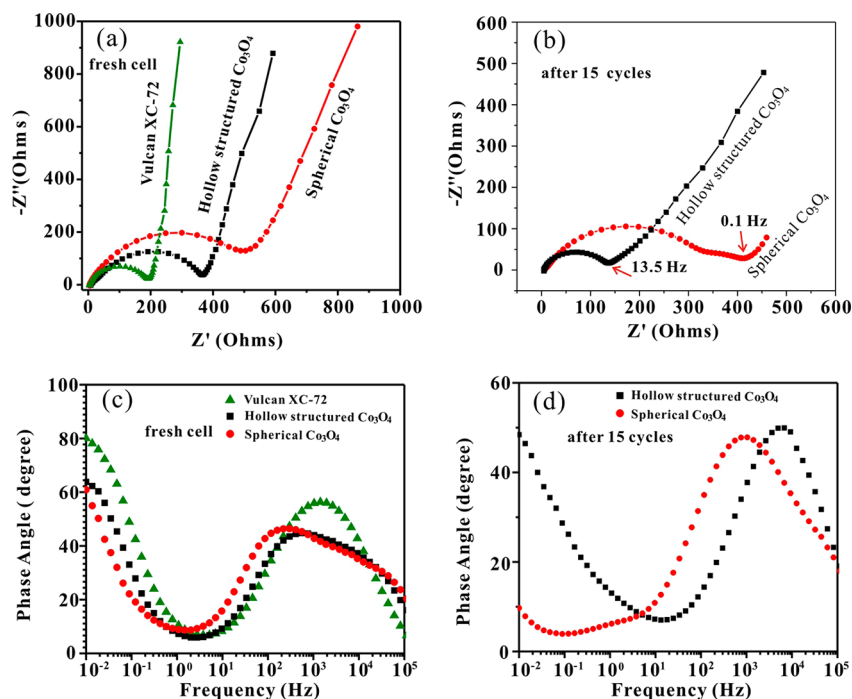


**Figure 4. Nyquist plots of different electrode materials. (a) Comparison of electrochemical impedance of hollow-structured $Co_3O_4$/C, special $Co_3O_4$/C, and Vulcan XC-72. (b) EIS of the $Co_3O_4$/C electrode after 15 cycles. (c, d) Bode plots of the corresponding EIS spectra.**

in high- and medium-frequency regions ($R_{ct}$) followed by an inclined line in low-frequency regions. (For an equivalent circuit model and the fitted impedance parameters see the Supporting Information Figure S4.) It can be seen clearly that the diameter of the semicircle for the hollow-structured $Co_3O_4$/C electrode ($R_{ct}$ = 385.8Ω) is much smaller than the spherical $Co_3O_4$/C one ($R_{ct}$ = 511.1Ω), indicating the hollow-structured $Co_3O_4$/C electrode exhibited better charge transfer performance and excellent conductivity. Figure 4b presents the EIS curves of the electrodes after 15 cycles. Obviously, after cycling, a small arc appeared in the media-frequency region except for the semicircle in the high-frequency region. It is reported that the semicircle in the high-frequency region is related to the SEI passivation film on the surface ($R_f$) and the arc at media-frequency is related to the charge transfer at the interface ($R_{ct}$).[48] The diameter of the semicircle for the hollow-structured $Co_3O_4$/C electrode decreased ($R_{ct}$ = 56.2) compared with the fresh cell, indicating the charge transfer resistance decreased apparently after 15 cycles. At the same time, the $R_{ct}$ of the spherical $Co_3O$/C electrode is about 86.5Ω, which is also much bigger than that of the hollow-structured $Co_3O_4$/C electrode. The SEI film resistance ($R_f$) of the hollow-structured and spherical $Co_3O_4$/C electrode is 126.9Ω and 320.8Ω, respectively. The low-frequency tail in the Nyquist curve represents the Warburg impedance, which reflects the solid-state diffusion of Li ions in the bulk anode materials.[49,50] It can be seen clearly that before cycling the slope angles of Vulcan XC-72 and both of the hollow-structured special $Co_3O_4$/C are closer to 90°, indicating the capacitive behavior of the materials. After 15 cycles, the slope angles for both samples are closer to 45°. However, the similar slope angle does not mean they have similar Li$^+$ transfer kinetics in the electrode materials. For the hollow-structured $Co_3O_4$/C electrode, the appearance of Li ions in solid-state diffusion at much higher frequency (13.5 Hz) than that of a spherical $Co_3O_4$/C electrode (0.1 Hz) indicates much faster charge transfer and Li ion migration through the surface film on the hollow-structured $Co_3O_4$/C electrode, resulting in better cycle stability and rate capability.

The structural stability of the hollow structures was verified by disassembling the coin cell and imaging the $Co_3O_4$/C structure after 50 cycles at 50 mA/g. Figure 4a−c show the HAADF-STEM images of several
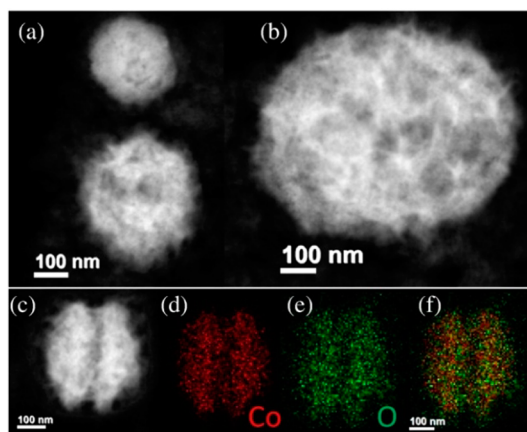


Figure 5. Microstructure of $Co_3O_4$/C after 50 cycles at a rate of 50 mA/g. (a−c) HAADF-STEM images of several nanoparticles. (d−f) EDX mapping of Co and O and its overlay.

aged composite nanoparticles. It can be seen clearly that the hollow structure was maintained even after intensive battery operation. The EDX mapping (Figure 5d−f) also confirms that Co and O still were homogeneously distributed within the nanoparticle. We attribute the stable performance during Li$^+$ intercalation and deintercalation of hollow $Co_3O_4$/C to its robust structure.

## CONCLUSIONS

In conclusion, a method of preparing hollow $Co_3O_4$/C nanoparticles has been developed by a very simple two-step solid-state synthesis process. During LIBs testing, the hollow $Co_3O_4$ exhibited excellent discharge capacity and durable performance when compared to nonhollow structures, likely due to the void spaces inside the particles (Figure 3c). Due to the nature of solid-state synthesis, this method represents a simple and cost-effective way for manufacturing hollow TMO nanoparticles and thus represents a promising future in large-scale LIB materials production. Further studies are ongoing to establish the relationship between the air flow rate and nanoparticle size distribution, the correlation between heating temperature and battery performance, the role of different transition metal precursors, and others. By optimizing these parameters, we believe that this facile synthetic method can be useful for large-scale LIB anode manufacture.

## METHODS

**Material Synthesis.** The hollow $Co_3O_4$/C material was synthesized *via* an impregnation−reduction method followed by an air-oxidation procedure. Namely, 1.61 g of $CoCl_2 \cdot 6H_2O$ was dissolved in ultrapure water, with 0.6 g of Vulcan XC72 added to the solution, which was ultrasonicated for 30 min to achieve homogeneity. A thick carbon slurry was obtained by repeated concentration using heat stirring and dissipation using sonication. After incubating for about 12 h under a vacuum oven at 60 °C, the dried sample was

ground, placed in a ceramic heating boat, and transferred to a tube furnace. Under forming gas (about 5% hydrogen in nitrogen) flow, $CoCl_2$/C is reduced to Co/C at 300 °C for 5 h. The Co/C nanoparticles with 40 wt % of Co metal were then obtained by cooling the precursor to room temperature under a nitrogen atmosphere. The Co/C nanoparticles were placed into the tube furnace again and heated to 400 °C with a heating rate of 1 °C/min in air atmosphere. The nanoparticles were incubated at 400 °C for 10 h to obtain mesoporous $Co_3O_4$ on the carbon support.

**Material Characterization.** Powder X-ray diffraction was performed by using an X'Pert PRO diffractometer, and diffraction patterns were collected at a scanning rate of 5°/min and with a step of 0.02°. Electron microscopy imaging was carried out using a Schottky-field-emission-gun Tecnai F20 scanning transmission electron microscope (STEM) operated at 200 keV. A high-angle annular dark field detector provided an incoherent projection image of the specimen with a signal intensity proportional to the amount of material and its atomic number, which is also known as $Z$-contrast. The energy-dispersive X-ray analysis was performed using an Oxford Instrument, at a beam current of about 1 nA. An EDX resolution of $1-5$ nm is routinely achieved with this setup. The material was stable under prolonged exposure to the electron beam (about $10-20$ min), which was verified by taking another image after EDX analysis.

**Electrochemical Measurement.** Electrochemical measurements were carried out in CR 2032 coin cells assembled in an argon-filled glovebox with lithium metal as the anode. The anodes consisted of 90 wt % active materials and 10 wt % polytetrafluoroethylene (PTFE) as a binder, which were rolled into a thin film. After drying under vacuum at 40 °C, the film was cut into circular electrodes with an area of 0.71 cm². The cut film was pressed onto nickel foam as one electrode. The counter electrode was Li metal. The two electrodes were separated by a polymeric material (Celgard 2320). The electrolyte was 1.0 M LiPF$_6$ in a 1:1 ratio of EC (ethylene carbonate) to DEC (diethylene carbonate). Galvanostatic charge/discharge of the coin cells were carried out at room temperature using an Arbin battery testing system with a constant discharge/charge current density varying from 0.05 to 2 A/g and a voltage range of +0.05 to +3.0 V at room temperature. Cyclic voltammetry testing of the cells was performed on a Solartron electrochemistry workstation at a scan rate of 0.05 mV/s. All the capacities were normalized to the mass of the Co$_3$O$_4$ in the active material. To exclude the capacity of Vulcan XC-72 in the measurement, a control experiment with only Vulcan XC-72 was carried out, and the actual capacity from Co$_3$O$_4$ is calculated based on the following equation.

$$C_{Co_3O_4} = \frac{Q_{total} - C_C \times m_C}{m_{Co_3O_4}} \tag{1}$$

where $C_{Co_3O_4}$ is the mass specific capacity of Co$_3$O$_4$ (the unknown), $Q_{total}$ is the measured coulomb charge, $m_{Co_3O_4}$ is the mass of Co$_3$O$_4$ (obtained from TGA, Supporting Information Figure S3), $C_C$ is the mass specific capacity of the carbon support (obtained via a control experiment, Figure 3c, the capacity of pure Vulcan XC-72), and $m_c$ is the mass of Vulcan XC72 (total material mass minus the mass of Co$_3$O$_4$).

Electrochemical impedance spectroscopy was measured on the coin cell using an AutolabPG302N electrochemical workstation. The amplitude of the ac signal applied to the electrode is 10 mV, and the frequency range is from 100 kHz to 0.1 Hz.

*Conflict of Interest:* The authors declare no competing financial interest.

*Supporting Information Available:* Additional figures (Figures S1–S4). This material is available free of charge *via* the Internet at http://pubs.acs.org.

## REFERENCES AND NOTES

1. Jayaprakash, N.; Jones, W. D.; Moganty, S. S.; Archer, L. A. Composite lithium battery anodes based on carbon@Co$_3$O$_4$ nanostructures: Synthesis and characterization. *J. Power Sources* **2012**, *200*, 53–58.
2. Wang, X.; Wu, X.-L.; Guo, Y.-G.; Zhong, Y.; Cao, X.; Ma, Y.; Yao, J. Synthesis and lithium storage properties of Co$_3$O$_4$ nanosheet-assembled multishelled hollow spheres. *Adv. Funct. Mater.* **2010**, *20*, 1680–1686.
3. Poizot, P.; Laruelle, S.; Grugeon, S.; Dupont, L.; Tarascon, J. M. Nano-sized transition-metaloxides as negative-electrode materials for lithium-ion batteries. *Nature* **2000**, *407*, 496–499.
4. Thackeray, M. M. Manganese oxides for lithium batteries. *Prog. Solid State Chem.* **1997**, *25*, 1–71.
5. Shi, X. Y.; Han, S. B.; Sanedrin, R. J.; Galvez, C.; Ho, D. G.; Hernandez, B.; Zhou, F. M.; Selke, M. Formation of cobalt oxide nanotubes: Effect of intermolecular hydrogen bonding between Co(III) complex precursors incorporated onto colloidal templates. *Nano Lett.* **2002**, *2*, 289–293.
6. Zhang, D. W.; Qian, A.; Chen, J. J.; Wen, J. W.; Wang, L.; Chen, C. H. Electrochemical performances of nano-Co$_3$O$_4$ with different morphologies as anode materials for Li-ion batteries. *Ionics* **2012**, *18*, 591–597.
7. He, T.; Chen, D. R.; Jiao, X. L.; Wang, Y. L. Co3O4 nanoboxes: Surfactant-templated fabrication and microstructure characterization. *Adv. Mater.* **2006**, *18*, 1078–1082.
8. Keng, P. Y.; Kim, B. Y.; Shim, I.-B.; Sahoo, R.; Veneman, P. E.; Armstrong, N. R.; Yoo, H.; Pemberton, J. E.; Bull, M. M.; Griebel, J. J.; Ratcliff, E. L.; Nebesny, K. G.; Pyun, J. Colloidal polymerization of polymer-coated ferromagnetic nanoparticles into cobalt oxide nanowires. *ACS Nano* **2009**, *3*, 3143–3157.
9. Chen, C.-H.; Abbas, S. F.; Morey, A.; Sithambaram, S.; Xu, L.-P.; Garces, H. F.; Hines, W. A.; Suib, S. L. Controlled synthesis of self-assembled metal oxide hollow spheres via tuning redox potentials: Versatile nanostructured cobalt oxides. *Adv. Mater.* **2008**, *20*, 1205–1209.
10. Qiao, R.; Zhang, X. L.; Qiu, R.; Kim, J. C.; Kang, Y. S. Morphological transformation of Co(OH)$_{(2)}$ microspheres from solid to flowerlike hollow core-shell structures. *Chem.—Eur. J.* **2009**, *15*, 1886–1892.
11. Ma, J. M.; Manthiram, A. Precursor-directed formation of hollow Co$_3$O$_4$ nanospheres exhibiting superior lithium storage properties. *Rsc Adv.* **2012**, *2*, 3187–3189.
12. Wang, X.; Tian, W.; Zhai, T. Y.; Zhi, C. Y.; Bando, Y.; Golberg, D. Cobalt(II,III) oxide hollow structures: fabrication, properties and applications. *J. Mater. Chem.* **2012**, *22*, 23310–23326.
13. Wang, Z. Y.; Zhou, L.; Lou, X. W. Metal oxide hollow nanostructures for lithium-ion batteries. *Adv. Mater.* **2012**, *24*, 1903–1911.
14. Ha, D. H.; Islam, M. A.; Robinson, R. D. Binder-free and carbon-free nanoparticle batteries: A method for nanoparticle electrodes without polymeric binders or carbon black. *Nano Lett.* **2012**, *12*, 5122–5130.
15. Wu, Z. S.; Ren, W. C.; Wen, L.; Gao, L. B.; Zhao, J. P.; Chen, Z. P.; Zhou, G. M.; Li, F.; Cheng, H. M. Graphene anchored with Co$_3$O$_4$ nanoparticles as anode of lithium ion batteries with enhanced reversible capacity and cyclic performance. *ACS Nano* **2010**, *4*, 3187–3194.
16. Ha, D.-H.; Islam, M. A.; Robinson, R. D. Binder-free and carbon-free nanoparticle batteries: A method for nanoparticle electrodes without polymeric binders or carbon black. *Nano Lett.* **2012**, *12*, 5122–5130.
17. Duan, B. R.; Cao, Q. Hierarchically porous Co$_3$O$_4$ film prepared by hydrothermal synthesis method based on colloidal crystal template for supercapacitor application. *Electrochim. Acta* **2012**, *64*, 154–161.
18. Guo, X.; Xu, W.; Li, S.; Liu, Y.; Li, M.; Qu, X.; Mao, C.; Cui, X.; Chen, C. Surfactant-free scalable synthesis of hierarchically spherical Co$_3$O$_4$ superstructures and their enhanced lithium-ion storage performances. *Nanotechnology* **2012**, *23*, 465401–465407.
19. Zhang, C. M.; Chen, J.; Zeng, Y.; Rui, X. H.; Zhu, J. X.; Zhang, W. Y.; Xu, C.; Lim, T. M.; Hng, H. H.; Yan, Q. Y. A facile approach toward transition metal oxide hierarchical structures and their lithium storage properties. *Nanoscale* **2012**, *4*, 3718–3724.

20. Wang, D.; Yu, Y.; Xin, H. L.; Hovden, R.; Ercius, P.; Mundy, J. A.; Chen, H.; Richard, J. H.; Muller, D. A.; DiSalvo, F. J.; Abruña, H. D. Tuning oxygen reduction reaction activity via controllable dealloying: A model study of ordered Cu$_3$Pt/C intermetallic nanocatalysts. *Nano Lett.* **2012**, *12*, 5230–5238.

21. Koh, S.; Strasser, P. Electrocatalysis on bimetallic surfaces: Modifying catalytic reactivity for oxygen reduction by voltammetric surface dealloying. *J. Am. Chem. Soc.* **2007**, *129*, 12624–12625.

22. Oezaslan, M.; Heggen, M.; Strasser, P. Size-dependent morphology of dealloyed bimetallic catalysts: linking the nano to the macro scale. *J. Am. Chem. Soc.* **2011**, *134*, 514–524.

23. Gan, L.; Heggen, M.; O'Malley, R.; Theobald, B.; Strasser, P. Understanding and controlling nanoporosity formation for improving the stability of bimetallic fuel cell catalysts. *Nano Lett.* **2013**, *13*, 1131–1138.

24. Liang, Y.; Li, Y.; Wang, H.; Zhou, J.; Wang, J.; Regier, T.; Dai, H. Co$_3$O$_4$ nanocrystals on graphene as a synergistic catalyst for oxygen reduction reaction. *Nat. Mater.* **2011**, *10*, 780–786.

25. Xia, X. H.; Tu, J. P.; Mai, Y. J.; Wang, X. L.; Gu, C. D.; Zhao, X. B. Self-supported hydrothermal synthesized hollow Co$_3$O$_4$ nanowire arrays with high supercapacitor capacitance. *J. Mater. Chem.* **2011**, *21*, 9319–9325.

26. Rakhi, R. B.; Chen, W.; Cha, D.; Alshareef, H. N. Substrate dependent self-organization of mesoporous cobalt oxide nanowires with remarkable pseudocapacitance. *Nano Lett.* **2012**, *12*, 2559–2567.

27. Liu, J.; Xue, D. F. Hollow nanostructured anode materials for Li-ion batteries. *Nanoscale Res. Lett.* **2010**, *5*, 1525–1534.

28. Trahey, L.; Vaughey, J. T.; Kung, H. H.; Thackeray, M. M. High-capacity, microporous Cu$_6$Sn$_5$-Sn anodes for Li-ion batteries. *J. Electrochem. Soc.* **2009**, *156*, A385–A389.

29. Cui, C.; Li, H.-H.; Liu, X.-J.; Gao, M.-R.; Yu, S.-H. Surface composition and lattice ordering controlled activity and durability of CuPt electrocatalysts for oxygen reduction reaction. *ACS Catal.* **2012**, *2*, 916–924.

30. Wang, J. Y.; Yang, N. L.; Tang, H. J.; Dong, Z. H.; Jin, Q.; Yang, M.; Kisailus, D.; Zhao, H. J.; Tang, Z. Y.; Wang, D. Accurate control of multishelled Co$_3$O$_4$ hollow microspheres as high-performance anode materials in lithium-ion batteries. *Angew. Chem., Int. Ed.* **2013**, *52*, 6417–6420.

31. Xu, X. L.; Zhang, X.; Sun, H.; Yang, Y.; Dai, X. P.; Gao, J. S.; Li, X. Y.; Zhang, P. F.; Wang, H. H.; Yu, N. F.; Sun, S. G. Synthesis of Pt-Ni alloy nanocrystals with high-index facets and enhanced electrocatalytic properties. *Angew. Chem., Int. Ed.* **2014**, *53*, 12522–12527.

32. Lou, X. W.; Archer, L. A.; Yang, Z. C. Hollow micro-/nanostructures: Synthesis and applications. *Adv. Mater.* **2008**, *20*, 3987–4019.

33. Titirici, M.-M.; Antonietti, M.; Thomas, A. A generalized synthesis of metal oxide hollow spheres using a hydrothermal approach. *Chem. Mater.* **2006**, *18*, 3808–3812.

34. Wang, W.; Dahl, M.; Yin, Y. Hollow nanocrystals through the nanoscale Kirkendall effect. *Chem. Mater.* **2013**, *25*, 1179–1189.

35. Ren, H.; Yu, R.; Wang, J.; Jin, Q.; Yang, M.; Mao, D.; Kisailus, D.; Zhao, H.; Wang, D. Multishelled TiO$_2$ hollow microspheres as anodes with superior reversible capacity for lithium ion batteries. *Nano Lett.* **2014**, 6679–6684.

36. Wang, D. L.; Lu, S. F.; Kulesza, P. J.; Li, C. M.; De Marco, R.; Jiang, S. P. Enhanced oxygen reduction at Pd catalytic nanoparticles dispersed onto heteropolytungstate-assembled poly(diallyldimethylammonium)-functionalized carbon nanotubes. *Phys. Chem. Chem. Phys.* **2011**, *13*, 4400–4410.

37. Wang, D. L.; Xin, H. L.; Wang, H. S.; Yu, Y. C.; Rus, E.; Muller, D. A.; DiSalvo, F. J.; Abruna, H. D. Facile synthesis of carbon-supported Pd-Co core-shell nanoparticles as oxygen reduction electrocatalysts and their enhanced activity and stability with monolayer Pt decoration. *Chem. Mater.* **2012**, *24*, 2274–2281.

38. Wang, D. L.; Xin, H. L. L.; Hovden, R.; Wang, H. S.; Yu, Y. C.; Muller, D. A.; DiSalvo, F. J.; Abruna, H. D. Structurally ordered intermetallic platinum-cobalt core-shell nanoparticles with enhanced activity and stability as oxygen reduction electrocatalysts. *Nat. Mater.* **2013**, *12*, 81–87.

39. Erlebacher, J.; Aziz, M. J.; Karma, A.; Dimitrov, N.; Sieradzki, K. Evolution of nanoporosity in dealloying. *Nature* **2001**, *410*, 450–453.

40. Ha, D.-H.; Moreau, L. M.; Honrao, S.; Hennig, R. G.; Robinson, R. D. The oxidation of cobalt nanoparticles into Kirkendall-hollowed CoO and Co$_3$O$_4$: The diffusion mechanisms and atomic structural transformations. *J. Phys. Chem. C* **2013**, *117*, 14303–14312.

41. Wang, C. M.; Baer, D. R.; Thomas, L. E.; Amonette, J. E.; Antony, J.; Qiang, Y.; Duscher, G. Void formation during early stages of passivation: Initial oxidation of iron nanoparticles at room temperature. *J. Appl. Phys.* **2005**, *98*, 094308–7.

42. Liu, X. H.; Yi, R.; Wang, Y. T.; Qiu, G. Z.; Zhang, N.; Li, X. G. Highly ordered snowflakelike metallic cobalt microcrystals. *J. Phys. Chem. C* **2007**, *111*, 163–167.

43. Liu, Q. Y.; Guo, X. H.; Li, Y.; Shen, W. J. Hierarchical growth of Co nanoflowers composed of nanorods in polyol. *J. Phys. Chem. C* **2009**, *113*, 3436–3441.

44. Zhong, Y. T.; Wang, X.; Jiang, K. C.; Zheng, J. Y.; Guo, Y. G.; Ma, Y.; Yao, J. N. A facile synthesis and lithium storage properties of Co$_3$O$_4$-C hybrid core-shell and hollow spheres. *J. Mater. Chem.* **2011**, *21*, 17998–18002.

45. Xia, X. H.; Tu, J. P.; Zhang, Y. Q.; Mai, Y. J.; Wang, X. L.; Gu, C. D.; Zhao, X. B. Freestanding Co$_3$O$_4$ nanowire array for high performance supercapacitors. *RSC Adv.* **2012**, *2*, 1835–1841.

46. Kaskhedikar, N. A.; Maier, J. Lithium storage ion carbon nanostructures. *Adv. Mater.* **2009**, *21*, 2664–2680.

47. Fang, Y.; Lv, Y. Y.; Che, R. C.; Wu, H. Y.; Zhang, X. H.; Gu, D.; Zheng, G. F.; Zhao, D. Y. Two-dimensional mesoporous carbon nanosheets and their derived graphene nanosheets: Synthesis and efficient lithium ion storage. *J. Am. Chem. Soc.* **2013**, *135*, 1524–1530.

48. Kang, Y. M.; Song, M. S.; Kim, J. H.; Kim, H. S.; Park, M. S.; Lee, J. Y.; Liu, H. K.; Dou, S. X. A study on the charge-discharge mechanism of Co$_3$O$_4$ as an anode for the Li ion secondary battery. *Electrochim. Acta* **2005**, *50*, 3667–3673.

49. Choi, B. G.; Hong, J.; Hong, W. H.; Hammond, P. T.; Park, H. Facilitated ion transport in all-solid-state flexible supercapacitors. *ACS Nano* **2011**, *5*, 7205–7213.

50. Mukaibo, H.; Momma, T.; Mohamedi, M.; Osaka, T. Structural and morphological modifications of a nanosized 62 atom percent Sn-Ni thin film anode during reaction with lithium. *J. Electrochem. Soc.* **2005**, *152*, A560–A565.